Research Article

Na Wang*, Jinsong Hu*, Jingru Li, Zhongfu Tan, Litong Dong, Nian Mei, and Haiyou Wang

Structural properties and reactivity variations of wheat straw char catalysts in volatile reforming

https://doi.org/10.1515/gps-2022-0084
received June 27, 2022; accepted October 01, 2022

Abstract: In this study, wheat straw char was prepared at 500°C and used as a catalyst (at 500–700°C) to reform the wheat straw volatiles. The char samples before and after reforming were characterized in terms of N_2 adsorption (BET area), Raman spectroscopy, Fourier transform infrared spectroscopy, proximate analysis, ultimate analysis, and inductively coupled plasma measurements. The surface morphology of the used char was analyzed by a scanning electron microscope. The results have revealed that following the reforming process, the carbon content increased from 69.2% to 71.7% (at 500°C), 73.9% (at 600°C), and 74.3% (at 700°C) and the fixed carbon content increased from 64.6% to 68.7% (at 500°C), 71.4% (at 600°C), and 72.4% (at 700°C). In contrast, the higher heating value of the used char remained unchanged. We observed a decrease in specific surface area (from 112.67 to 7.93 $m^2 \cdot g^{-1}$), but an increase in char defects and functional groups following the reforming process (at 600°C) served to maintain catalytic activity, as shown in a second reforming test. Our results suggest that surface defects and functional groups are the main factors contributing to char reactivity.

Keywords: wheat straw char, volatile reforming, defects, functional groups, reactivity

*** Corresponding author: Na Wang,** State Grid Economic and Technological Research Institute Co., Ltd., Beijing, 102209, China; North China Electric Power University, Beijing, 102206, China, e-mail: wangna1203@alumni.tongji.edu.cn
*** Corresponding author: Jinsong Hu,** State Grid Economic and Technological Research Institute Co., Ltd., Beijing, 102209, China, e-mail: hujinsong@chinasperi.sgcc.com.cn
Jingru Li, Litong Dong, Nian Mei, Haiyou Wang: State Grid Economic and Technological Research Institute Co., Ltd., Beijing, 102209, China
Zhongfu Tan: Department of Economics and Management, North China Electric Power University, Beijing, 102206, China

1 Introduction

Biomass pyrolysis is considered a viable technology for obtaining products with increased value and wide-ranging applications [1]. Pyrolysis is a chemical process whereby biomass is thermally decomposed without a supply of air or other oxygen to generate gaseous, liquid, and solid products. The gas phase product has a high calorific value [2], while the oily liquid products contain water, alcohols, organic acids, ketones, aldehydes, ethers, and phenols. As such, the liquid fraction is highly oxygenated and acidic, making it unfavorable in terms of utilization [3]. Given this technological constraint, extensive research has been conducted on the conversion of pyrolysis liquids to permanent gases (such as CH_4, CO, and H_2) or more stable deoxygenated oils. A progressive upgrade of the pyrolysis products should involve the application of catalysis [4].

Char is a porous carbonaceous by-product obtained in pyrolysis. Char and char-supported metallic catalysis have been the focus of recent studies [5–7] due to their low cost, high-specific surface area, and flexibility in determining product composition. The catalytic pyrolysis process is complex as it involves the primary degradation of biomass and secondary gas-phase and gas–solid reactions [8]. Moreover, the char structure and the presence of alkali, alkaline earth, and other metallic species (AAEMs) can influence reactivity. Work to date has considered the effect of AAEMs content on catalytic activity [9]. It has been shown that Ca can react with the carboxyl groups present on the char surface to form $-(COO)_2Ca$ species (Eq. 1), which are very active in enhancing gasification [10,11]. The presence of K and Na can increase the breakdown of large aromatic ring systems by enhancing the formation of M–C–O and C(O) as reactive intermediates during the gasification of coke [12].

$$Ca^{2+} + 2[-(COOH)] \rightarrow -(COO)_2Ca + 2H^+ \quad (1)$$

At higher temperatures, AAEMs evaporate [13], but char still exhibits significant catalytic activity [14]. Consequently, the role of char properties on the volatile–char

processes requires further exploration to establish a quantitative relation between structure and performance in order to enhance efficiency and extend applicability [15]. This is complicated by the possible variations in char characteristics and volatile composition. We have taken the approach of tracking the changes in the char after reaction and the volatile composition with and without char.

To date, the majority of studies have focused on coal [16], particularly the effects of volatile–char interactions on the structure and reactivity of char during high-temperature pyrolysis or gasification [17]. There is no reported data on the influence of char on volatile composition. This study examines the changes in char structural and composition characteristics and volatile composition to reveal the possible reactions taking place during volatile–char interactions. The biomass char prepared in advance from pyrolysis (at 500°C) was subjected to volatile–char interactions in a fixed-bed reactor with volatiles generated from wheat straw pyrolysis, considering the effects of volatile–char interactions over an extended temperature range (500–700°C). The explicit purpose of this research is to establish catalytic activity for pyrolysis char in the reforming of pyrolysis volatiles as a means of determining the potential utilization of the char as a catalyst. We apply a range of characterization techniques before and after the pyrolysis-reforming process to monitor critical changes in char structure and composition.

Table 1: Proximate analysis and composition of wheat straw sample for pyrolysis

Proximate analysis (air dry basis, wt%)				
M[a]	**Ash**	**V[b]**	**FC[c]**	
7.9 ± 0.23	**5.2 ± 0.76**	**71.5 ± 1.21**	**15.4 ± 0.02**	
Ultimate analysis (air dry basis, wt%)				**HHV (air dry basis, MJ·kg^{-1})**
C	**H**	**N**	**O**	
45.0 ± 2.72	5.8 ± 0.12	0.3 ± 0.01	48.9 ± 0.96	17.7 ± 0.21

[a]Water content; [b]Volatile; [c]Fixed carbon.

2 Materials and methods

2.1 Materials

The wheat straw was supplied by Dittmannsdorfer Milch GmbH in Kitzscher, Germany, and milled to pass through a sieve of 1 mm. The proximate analysis, ultimate analysis, and higher heating value (HHV) of the wheat straw sample are demonstrated in Table 1.

Pyrolysis of wheat straw in nitrogen was used to produce biomass char at 500°C; wheat straw samples were heated from ambient temperature to 500°C at a rate of 10°C·min^{-1} and maintained at the final temperature for 0.5 h. The reforming experiments were conducted in a fixed-bed reactor, as illustrated in Figure 1. The volatiles produced from the pyrolysis reactor (at 500°C) contacted the hot char in the reforming reactor.

The temperature of the reforming reactor was increased to 500°C, 600°C, and 700°C. Four char samples were obtained as shown in Table 2. PC-500 stood for the char of wheat straw produced at 500°C. PRC-500, PRC-600, PRC-700 stood for the PC-500 after reforming process at 500°C, 600°C, 700°C, respectively.

2.2 Gas analysis

After cooling down the reactor, the effluent gas was collected into a gas bag and analyzed for H_2, CO, CO_2, CH_4,

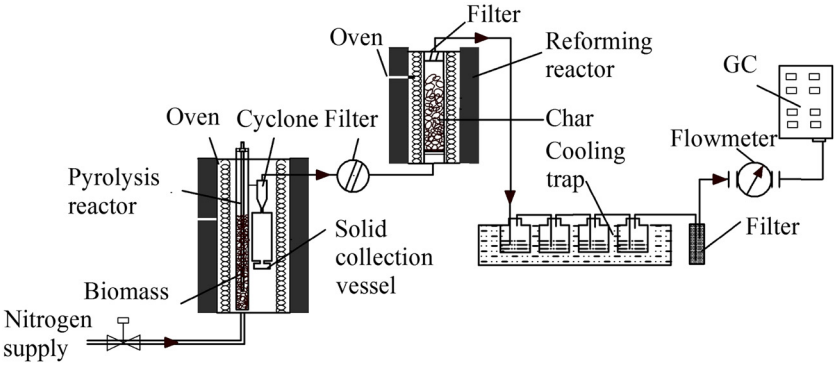

Figure 1: Diagram of the experimental apparatus.

Table 2: Overview of the investigated char samples

Char sample	Pyrolysis temperature (°C)	Reforming temperature (°C)
PC-500	500	no
PRC-500	500	500
PRC-600	500	600
PRC-700	500	700

C_2H_6, C_2H_4, and C_3H_6 using an Agilent 7890A type gas chromatography (GC; Agilent, USA) [18]. The gas yield obtained from GC measurement is based on volume but is expressed in terms of mass in this study.

2.3 Char characterization

2.3.1 Composition of the char

Char samples were analyzed with a Raman spectrometer (Renishaw Ltd., UK) [19]. The laser power was set at ~20 mW.

The char samples were determined by Fourier transform infrared (FTIR) spectroscopy (BrukerVertex 70, EQUINOXSS/HYPER, Germany) in an Attenuated Total Reflectance (ATR) mode. The FTIR data were subjected to OPUS software (Bruker, Germany) analysis. The spectral region 570–4,000 cm^{-1} was recorded with a resolution of 0.5 cm^{-1}. The vibrational bands were identified using the FTIR database [20] and standard compound measurements.

Elemental analysis of solids was performed in triplicates using a Vario EL elemental analyzer (Elementar, Germany) to obtain the C, H, and N content. The oxygen content was derived by difference. The HHV was determined using an IKA C5000 bomb calorimeter.

To measure the concentrations of AAEMs and additional typical inorganic elements contained in the char, the milled char samples were digested [21], in an ultra Clave-IV high pressure microwave (MWS Vertriebs GmbH, Germany), with 65% nitric acid at 250°C, 115 bar for 1 h for biomass samples and at 260°C, 140 bar for 2 h for char samples. The resultant solution was stored at room temperature and then analyzed by an ICAP 6300 inductively coupled plasma (ICP)-OES (Thermo Scientific, USA).

2.3.2 Microstructure of char

The Brunauer–Emmett–Teller (BET) surface area, micropore surface, external surface area, average diameter, and total volume of the char samples were analyzed by N_2 adsorption and desorption isotherms on an ASAP-2020M analyzer (Micromeritics, USA).

The BET equation was used to calculate the specific surface area. The pore size distribution by volume (dV_{pore}/dV_p) was calculated according to the BJH theory [22]. The external surface area (S_{ext}) and micropore volume (V_{micro}) were obtained using the t-plot method [23]. The microporous surface area (S_{mic}) was determined based on the differences between S_{BET} and S_{ext} [24].

The surface morphology of char samples was analyzed using a field emission scanning electron microscope (SEM) (Quanta 2000, FEI, USA).

2.4 Products and their yields

The effect of reforming temperature on product yield is summarized in Figure 2. Gas yields increased but liquid yields decreased with increasing process temperature. In addition, the yield of all gases in the reforming process was higher than that from the pyrolysis process. The opposite trend was observed for the yield of liquids.

Figure 3 shows the effects of reforming temperature on the yields of CO, CO_2, H_2, CH_4, C_2H_4, and C_2H_6. It is obvious that the yield of all gaseous products increases after the reforming process. The yield of CO reached 11.6 wt% when the reforming temperature was 600°C, and the yield of CO_2 decreased over the temperature interval of 500–700°C. This may be caused by CO_2 reacting with char to produce CO when the reforming temperature was set at 600°C.

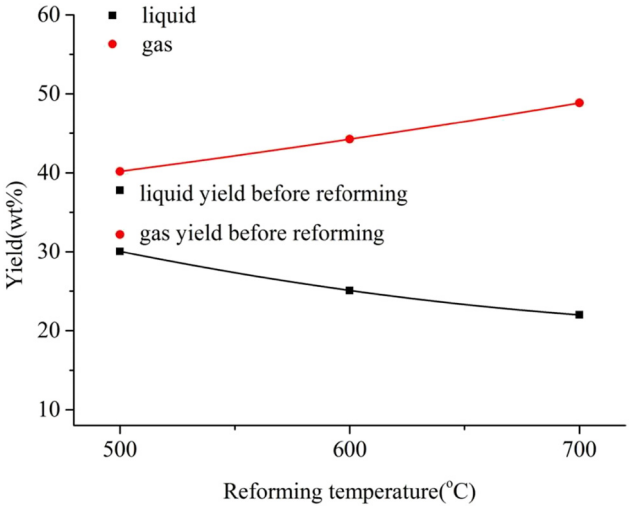

Figure 2: The effect of reforming temperature on liquid and gas yields.

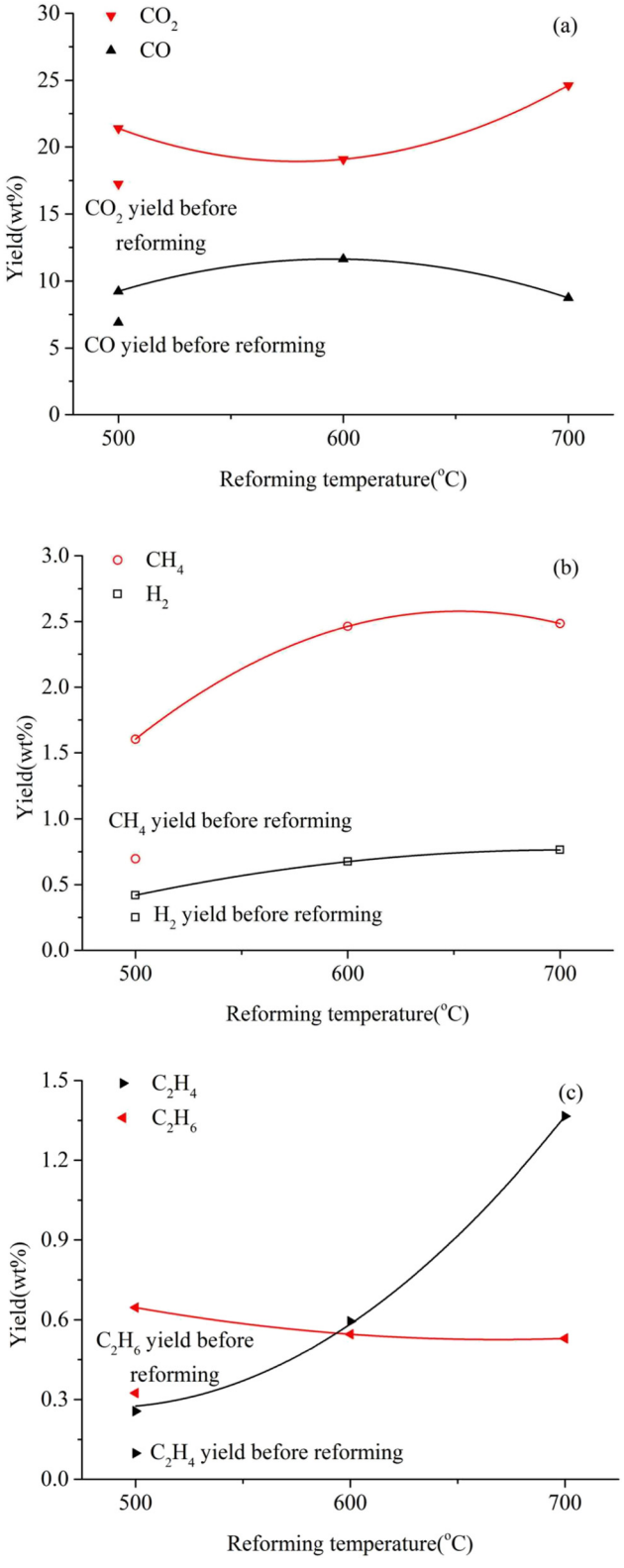

Figure 3: The effects of reforming temperature on the yields of different gases: (a) CO and CO_2; (b) H_2 and CH_4; (c) C_2H_4 and C_2H_6.

As the reforming temperature increased, the yields of H_2, CH_4, and C_2H_4 also increased, but we observed a decrease in the C_2H_6 yield. This response may be due to thermochemical reactions between tar, char, and syngas at higher temperatures [25].

$$C_nH_m + pH_2O \rightarrow C_{n-p}H_y + pCO + (p + (m - y)/2)H_2 \quad (2)$$

$$C_nH_m + nCO_2 \rightarrow 2nCO + (m/2)H_2 \quad (3)$$

Char can react with syngas to generate other gases (e.g., H_2 and CH_4). In addition, tar can be cracked into gas components during a reforming process over the char.

2.5 Char characterization

2.5.1 Chemical analyses of char

The ultimate and proximate analysis and HHV of the char samples are shown in Table 3. The results demonstrated that the char was richer in FC, A, C, and HHV and poorer in H and O after the reforming process. This may result from the donation of H and O from the char to form H_2O, H_2, CO_2, alkanes (CH_4, C_2H_6), and alkenes (C_2H_4, C_3H_6) during the reforming process, which constitutes a large proportion of the reforming gases and results in the enrichment of char with carbon [26]. An increase in reforming temperature can result in the release of H and O, leading to a higher FC, ash, and C content; as a result, HHV remains largely unchanged due to the balance of H loss and C increase. This phenomenon is in agreement with an increasing H_2 concentration at higher reforming temperatures [13].

The concentration of mineral elements is shown in Table 4.

As shown in Table 4, K and Na content decreased after the reforming process, mainly due to evaporation at higher temperatures. In contrast, the content of Ca and Si increased. In the case of PRC-500, all the elements (with the exception of Si) showed a slight decrease compared with PC-500, which may be due to incomplete evaporation of volatile matter in the char and carbon deposition on PRC-500. The elements Ca, Mg, Fe, and P can evaporate to varying degrees along with volatiles [27]. Higher reforming temperatures (600°C and 700°C) should favor the evaporation of volatile matter.

After the reforming process, the fixed carbon of the char samples was raised from 68.7% to 71.7%, falling within the range of medium to high fixed carbon coal

Table 3: Chemical analyses of char samples

Char samples	wt%								Aromatic ratio		HHV (kJ·g)
	M (ar[a])	V (ar)	FC (ar)	Ash (ar)	C (d[b])	H (d)	N (d)	O[c] (d)	H/C	O/C	
PC-500	4.0	16.0	64.6	15.5	69.2	2.9	0.8	17.1	0.50	0.25	26.03
PRC-500	3.2	8.9	68.7	19.2	71.7	2.4	0.8	14.4	0.40	0.20	26.13
PRC-600	2.7	6.4	71.4	19.5	73.9	1.7	0.9	12.5	0.28	0.17	25.12
PRC-700	2.8	4.6	72.4	20.2	74.3	0.9	1.1	11.9	0.15	0.16	25.75

[a] Water content; [b]Dry basis; [c]Determined by difference.

Table 4: The AAEMs and some typical inorganic element content of char samples (wt%)

Element treatment	Ca	K	Mg	Na	Fe	P	Si
PC-500	0.94	3.79	0.17	0.25	0.014	0.11	4.67
PRC-500	0.93	3.49	0.16	<0.02	0.013	0.09	5.94
PRC-600	1.03	3.05	0.17	<0.02	0.011	0.11	6.54
PRC-700	1.24	3.64	0.20	<0.02	0.015	0.12	6.49

(65.00–75.00%) [28]. Calcium carbide (CaC_2) is an important chemical source for acetylene (C_2H_2) and ethylene (C_2H_4). In the industrial production of calcium carbide (Eq. 1), metallurgical coke is the main raw material, consisting of fixed carbon (>84%) and ash (<14%) [29]. Taking account of scarcity, associated pollution, and the high price of coal, char from the reforming process may serve as a substitute for metallurgical coke, following some simple ash-washing processes. In order to increase the fixed carbon content, the char may be washed using the protocol reported previously [30].

$$CaO + 3C \rightarrow CaC_2 + CO \quad (4)$$

The HHV of the char was 25.12 $kJ \cdot g^{-1}$ or higher after reforming, which is comparable to high calorific value coal (>24.01 $MJ \cdot kg^{-1}$) [28]. With ultra-low total moisture (≤6.0%) and low-medium ash (10.01–20.00%) [28], the char is suitable for utilization as solid fuel.

2.5.2 Chemical structure of char

Guided by relevant literature [31–36], Raman spectra were collected in the 800–1,800 cm^{-1} region and curve-fitted with 10 Gaussian bands. An example of spectral deconvolution is presented in Figure 5 for char prepared from biomass pyrolysis in N_2 at 500°C.

As displayed in Figure 4, peaks denoted as G_R, G, V_R, V_L, S, and D are the six main bands that provide structural information for char. It has been well-documented [32] that I_G is the area of the G band that represents graphite-like carbon, I_D is the area of the D band that represents defect structures composed of large aromatic ring systems with at least six fused rings, and I_S is the area of the S band that represents sp^3-rich structures, including alkyl–aryl C–C and methyl carbon dangling from an aromatic ring. In addition, $I_{(GR+VL+VR)}$ is the total area of the ($G_R + V_L + V_R$) bands that represent typical structures in amorphous carbon, comprising small aromatic ring systems (less than six fused rings).

Figure 5 demonstrates the Raman band ratios I_S/I_G, $I_{(VR+VL+GR)}/I_D$, and I_D/I_G for the char sample from the biomass pyrolysis and char samples at three different reforming temperatures.

Taking the data in Figure 5b, the ratio $I_{(VR+VL+GR)}/I_D$ is a broad semi-quantitative reflection of the ratio of small-to-large aromatic ring systems in char. The $I_{(VR+VL+GR)}/I_D$ ratio decreases as the reforming temperature increases. This may be attributed to the fact that low temperatures favor the incomplete polymerization of small aromatic compounds with alkyl groups, resulting in a high amount of small aromatic ring systems in amorphous char [32]. During the reforming process, smaller aromatic ring systems are replaced by larger aromatic ring systems [37–39]. At a reforming temperature of 500°C, the $I_{(VR+VL+GR)}/I_D$ ratio is higher relative to the pyrolysis char without the reforming process. This may be attributed to the loss of volatiles and the accumulation of tar molecules (small aromatic ring structures).

Both I_S/I_G and I_D/I_G ratios pass through a maximum with increasing reforming temperature, as demonstrated in Figure 5a and c. The increase in I_S/I_G from 500°C to 600°C suggests an enhanced formation of alkyl–aryl C–C bonds caused by crosslinking reactions, possibly following decarboxylation or loss of other oxygen-containing functional groups. The decline over the temperature interval of 600–700°C can be accounted for in terms of Calkyl–Caryl structure formation that, in turn, generates small aromatic ring systems.

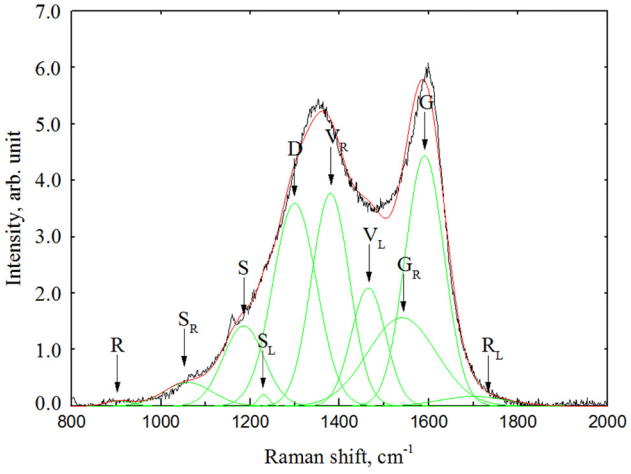

Figure 4: Curve-fitting of Raman spectra of the PC-500.

A similar increase in I_D/I_G over the temperature range of 500–600°C indicates a relative increase in the concentrations of aromatic rings containing at least six fused benzene rings. This can indicate the growth of aromatic rings and dehydrogenation of hydroaromatics in the char at this pyrolysis temperature range.

At 700°C, further ring condensation can generate additional large aromatic ring systems (≥6 fused benzene rings), characterized by the Raman D band. The accompanying decrease in "defect" structures, for example, due to continuous ring expansion, serves to reduce Raman D band intensity. The net effect is a decrease in I_D/I_G at the higher reforming temperature, as shown in Figure 5c. The I_D/I_G ratio can be used to characterize surface defect density, where a higher value reflects an increase in potential

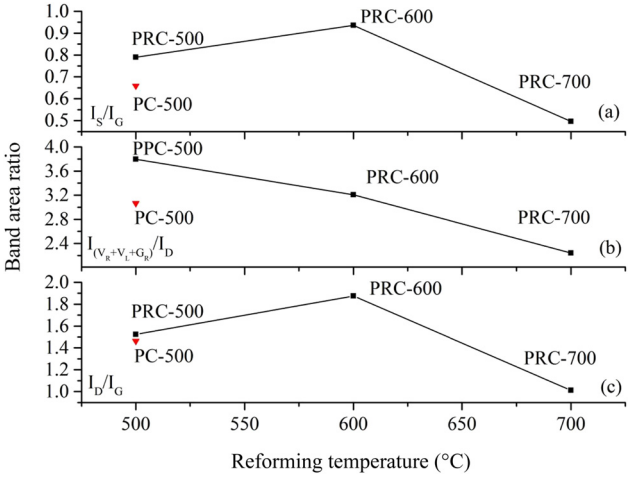

Figure 5: Raman band ratios as a function of reforming temperature for the pyrolysis and reforming chars from wheat straw: (a) I_S/I_G, (b) $I_{(VR+VL+GR)}/I_D$, and (c) I_D/I_G.

active sites [40]. Theoretically, breaking a chemical bond to generate atoms with lower coordination states is conducive to the formation of active sites. As shown in Figure 5c, the I_D/I_G of the char from reforming at 600°C is highest, indicating that char left from the reforming process at 600°C bears the most active sites. The active sites, as opposed to all surface sites, are responsible for heterogeneous catalytic reactions [41–43]. Surface defects allow the increased exposure of active edge sites by forming cracks on the surface, with a resultant marked enhancement of catalytic performance [44]. The results suggest that char formed during the reforming process at 600°C should exhibit the highest catalytic activity.

2.5.3 Char functional groups

The FTIR results of the four char samples are displayed in Figure 6.

At a reforming temperature of 500°C, there was little change in the peaks except for a decrease in the conjugated aromatic ring C=C stretching or conjugated aromatic carbonyl/carboxyl C=O stretching vibration (1,605 cm^{-1}) [45]. In contrast, almost all the functional group peaks were removed when the reforming temperature was elevated to 700°C. The loss of functionality and the decrease in the ratio of small-to-large aromatic ring systems (and defect density, as demonstrated in Figure 6b and c) indicate that high reforming temperatures (≥700°C) can cause the char to lose reactivity.

Following the reforming process at 600°C, a loss of alcohol/phenolic –OH groups (at 3,348 cm^{-1} [50]) and C=C or C=O groups (at 1,605 cm^{-1}) was observed. This implies that the C–OH and C=C or C=O linkages are not stable, which may be explained by decarboxylation or loss of oxygen-containing functional groups, as revealed in Table 3. The bands for aliphatic chains, such as CH_2 and CH_3 groups (1,371 and 1,400 cm^{-1}, respectively) [46], and the bands corresponding to aromatic HCC (H–C–C) rocking vibrations and aromatic bending modes in condensed and aromatic ring systems (between 700 and 900 cm^{-1}) [46] remained largely unchanged. The increase in the band for C–O or Si–O stretching vibration (1,074 cm^{-1}) [46] is associated with aldehydes and/or ketones since no detectable hydroxyl –OH group band is found within the range 3,000–3,600 cm^{-1} [47,48]. These oxygen functional groups play an important role in fixing tar molecules onto the char surface by influencing dispersive/repulsive interactions.

The results of Raman and FTIR analysis indicate that the char after use in the reforming process at 600°C still exhibits high reactivity. To establish the reactivity of the

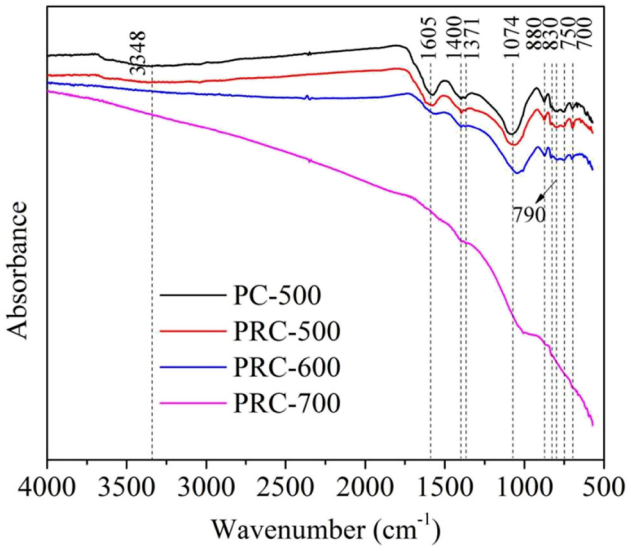

Figure 6: FTIR spectra of the raw char and char after the reforming process.

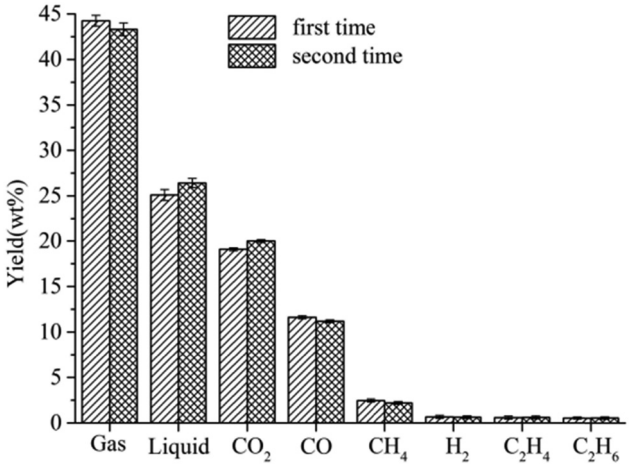

Figure 7: Reforming yield and product distribution with char used the first time and second time in the reforming process at 600°C.

used char after reforming at 600°C, the char that remained in the reforming reactor was used as a catalyst again in a subsequent new batch of volatile reforming reactions. The results are presented in Figure 7.

As shown in Figure 7, when the char after reforming at 600°C was reused, the resultant products changed very slightly; for example, the gas yield only decreased from 44.3 to 43.3 wt% and the liquid yield increased from 25.1% to 26.4%. In the case of the gaseous products, we observed a slight increase in CO_2 yield (from 19.1% to 20.1%); the yields of CH_4, CO, H_2, C_2H_4, and C_2H_6 were largely unchanged. These results establish that the char after use at 600°C in the reforming process retained catalytic reactivity for the volatile reforming process.

2.6 Microstructure of char

2.6.1 Char physical structure

The porosity characteristics of the char are presented in Table 5. The BET surface area of pyrolysis char obtained in this study is significantly higher than some commonly employed natural materials (e.g., 5–20 $m^2 \cdot g^{-1}$ dolomites) [36,49]. The total pore volume of the pyrolysis char is 0.0647 $cm^3 \cdot g^{-1}$, with a micropore volume of 0.0378 $cm^3 \cdot g^{-1}$.

According to the IUPAC definition, adsorbent pores can be divided into three groups: macropores (>50 nm), mesopores (2–50 nm), and micropores (diameter < 2 nm). The average diameter of the pyrolysis char is 2.30 nm, suggesting that it is composed of mesopores and micropores.

Considering the data in Table 5, BET surface (S_{BET}), micropore surface area (S_{mic}), and external surface area (S_{ext}) decreased dramatically, with an accompanying drop in V_{mic} and V_{total} but the average pore diameter (D_{aver}) increased. The reforming product yields displayed in Figures 3 and 7 suggest that the liquid and gas yields are more related to temperature than the char microstructure. However, PRC-600 has a relatively higher S_{mic} and V_{mic} and smaller D_{aver} than PRC-500 and PRC-700, indicative of a greater micropore and mesopore content. We note that the products changed little when the char used at 600°C served again as a catalyst in the reforming process. The results suggest that the BET surface is not a dominant factor in the reactivity of the char.

Figure 8 shows the nitrogen adsorption/desorption isotherm and pore size distribution of the char samples before and after the reforming process. The adsorption/desorption isotherm for PC-500 (Figure 8a) can be classified as a type I isotherm, typical of microporous materials. The open curve is indicative of a pores distribution in the range of 2–10 nm where adsorption is facilitated and desorption restricted. The adsorption/desorption isotherm for PRC-500 and PRC-600 can be classified as type III, typical of weak interaction materials, and the H3 hysteresis loop suggests slit pore formation caused by the accumulation of flaky particles. The adsorption/desorption isotherm of PRC-700 can be classified as a type VI, consistent with multilayer adsorption materials, and the H4 hysteresis loop suggests slit pores produced by the layered structure.

As shown in Figure 8a, the relative pressure covers the range 0.05–0.99. The steep slope of the curve at a lower relative pressure (p/p_0 < 0.1) is followed by a

Table 5: Porosity characteristics of the char samples

Sample	S_{BET} ($m^2 \cdot g^{-1}$)	S_{mic} ($m^2 \cdot g^{-1}$)	S_{ext} ($m^2 \cdot g^{-1}$)	V_{mic} ($cm^3 \cdot g^{-1}$)	V_{total} ($cm^3 \cdot g^{-1}$)	D_{aver} (nm)
PC-500	112.67	99.39	13.28	0.0378	0.0647	2.30
PRC-500	4.21	3.14	1.07	0.0015	0.0037	14.01
PRC-600	7.93	6.42	1.51	0.0029	0.0030	7.96
PRC-700	3.78	1.04	2.74	0.0018	0.0079	18.17

S_{BET}, S_{mic}, S_{ext}, V_{mic}, V_{total}, and D_{aver} represent BET surface area, micropore surface area, external surface area, micropore volume, total volume, and average diameter, respectively.

gradual uptake over the 0.1–0.9 range to attain a plateau value. The initial (steep) part of the isotherm indicates micropore filling (instead of surface coverage), while the lesser slope to attain the plateau assumes the possibility of multilayer adsorption on the external surface. The final hysteresis loop is consistent with mesopore content. Thus, the pyrolysis char can be considered a microporous solid with a small external area.

As demonstrated in Figure 8b–d, both the surface area and volume of the char significantly decreased after the reforming process. It can also be noted that S_{mic}/S_{BET} and S_{mic}/V_{total} decreased along with the reduction of surface area and volume. The average diameter of all the reforming chars exceeds 9 nm and reaches mesopore dimensions. This is mostly due to the destruction of small pores, including micropores and some mesopores, during

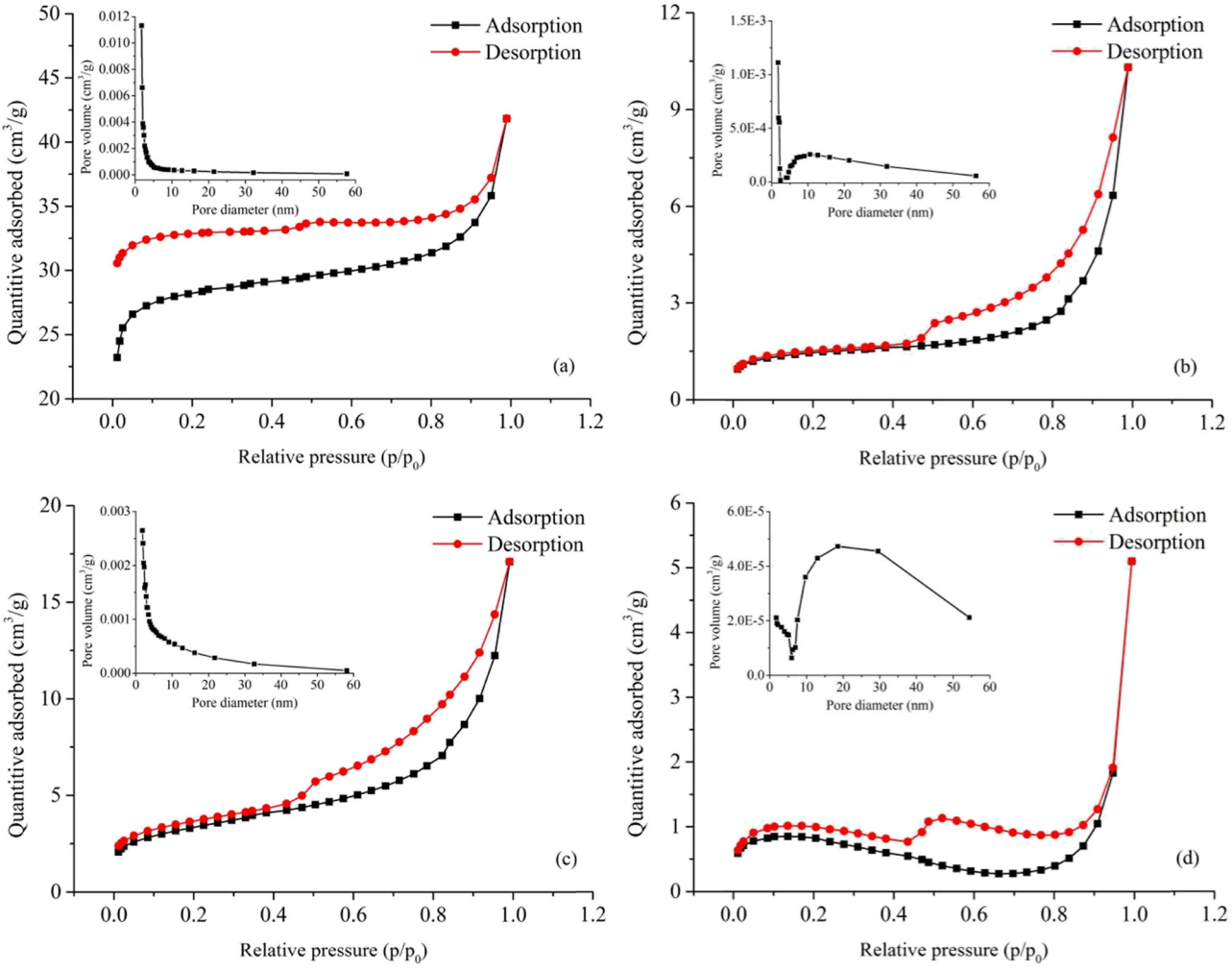

Figure 8: Adsorption/desorption isotherms of N_2 and pore distribution: (a) PC-500, (b) PRC-500, (c) PRC-600, and (d) PRC-700.

the reforming process. Compared with the reforming char at 500°C, the char reformed after 600°C has a slightly larger surface area and volume, which we attribute to the higher temperature facilitating evaporation (or oxidation) of organic volatiles. The decrease in the surface area and volume at a reforming temperature of 700°C may be caused by carbon deposition with consequent pore blockage.

The pore size distributions of the char samples are also displayed in Figure 8, where the pores of sample PC-500 are less than 5 nm (micropores; Figure 8a). Most of the pores shown in Figure 8b distributed around 10 nm are in the mesopore range. As shown in Figure 8c, most of the pores are less than 10 nm, suggesting a micropore and mesopore component. The data presented in Figure 8d are consistent with pores between 10 and 30 nm, i.e., mesopores. These results suggest that mesopores were readily formed during the reforming process.

2.6.2 Char morphology

Figure 9 shows SEM morphology images of the four different char samples. The samples exhibit four types of surface morphology: large plane structures, laminated fractures, abrasive surfaces, and clusters formed by the accretion of small globular substances. SEM characterization illustrates that PC-500 is composed of a dense and abrasive surface dispersed with some small clusters. After the reforming process, the laminated fracture does not feature and is replaced by an abrasive surface; the char surfaces of PRC-500, PRC-600, and PRC-700 appear regular and fluffy. This is particularly apparent at the highest reforming temperature (700°C). According to our studies, PC-500 char can achieve a higher BET surface area ($112.67\ m^2 \cdot g^{-1}$), which may contribute to its laminated fracture. The increase of abrasive surface character and cluster structure may also increase surface area, but we

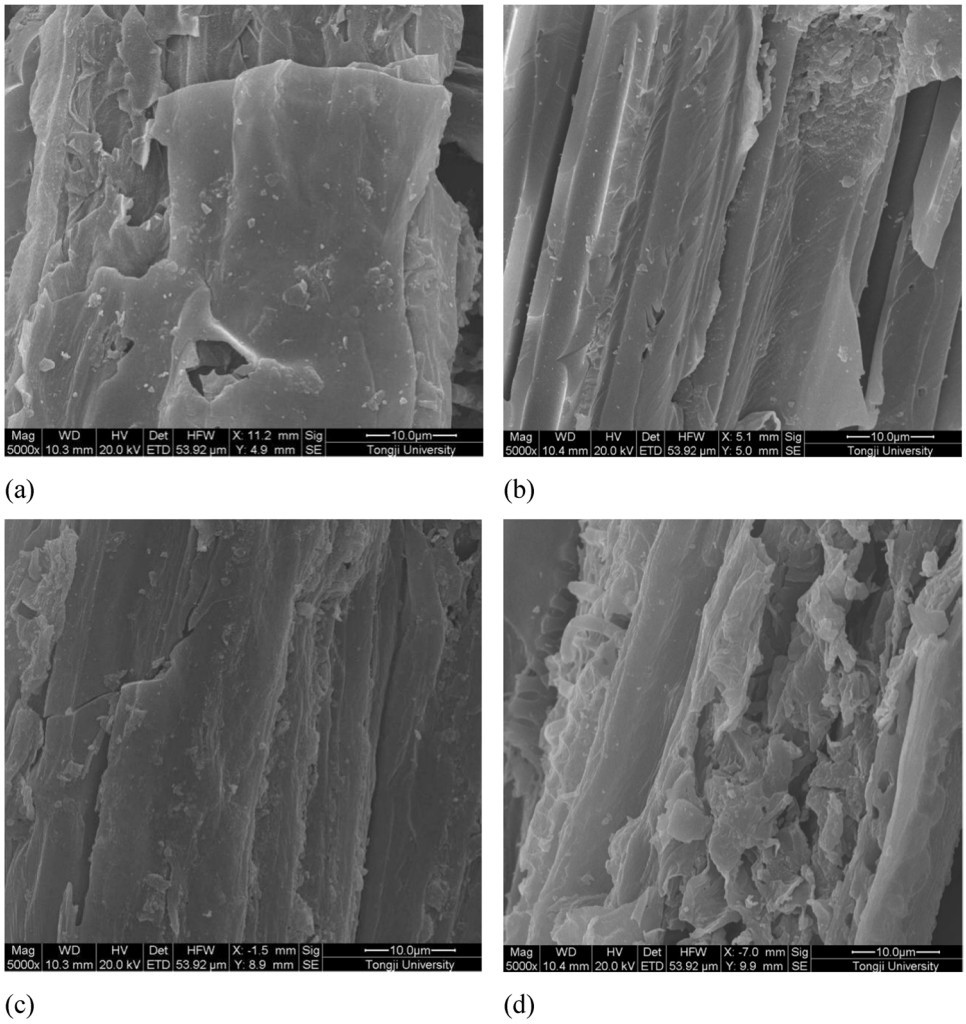

Figure 9: SEM micrographs of raw char and char after reforming process: (a) PC-500, (b) PRC-500, (c) PRC-600, and (d) PRC-700.

observe a decrease in BET values after the reforming process. This may be explained by the loss of laminated fractures, which were more important in determining area than abrasive surfaces and clusters.

3 Conclusions

The formation mechanism of pyrolysis char and reformed char has been investigated in terms of structure and composition using a range of techniques (BET, SEM, Raman, FTIR, chemical analyses [ultimate analysis, proximate analysis, and HHV], ICP, and SEM-EDS). The conclusions are summarized as follows:

1. The pyrolysis char exhibits a high surface area (112.67 $m^2 \cdot g^{-1}$) but after the reforming process, it decreases to <8 $m^2 \cdot g^{-1}$. The char functionality includes nitrogen functional groups (N═C), carbon functional groups (C═C), and oxygen functional groups (C–O, C═O, –OH, and Si–O). The char after reforming at 600°C shows the highest I_D/I_G, suggesting a greater number of active sites.
2. The AAEMs and inorganic element content in char samples include Ca, K, Mg, Na, Fe, P, and Si. The functional groups and AAEMs and other metallic elements (with the exception of Na) changed very little before and after reforming at 500°C and 600°C.
3. The char after reforming at 600°C was used again in a subsequent reforming process at 600°C, and the product yield showed very little change. This implies that the dominant factors determining catalytic reactivity are the functional groups, the active sites, the AAEMs, and other typical metallic elements during the reforming process; the influence of the surface area appears to be less significant.
4. Conducting the reforming process at 700°C resulted in a loss of functional groups and a dramatic drop in I_D/I_G. In order to retain catalytic activity and efficiency, the reforming temperature should be set at 600°C.

Funding information: The authors state no funding involved.

Author contributions: Na Wang: writing – original draft, writing – review and editing. Jinsong Hu: methodology. Jingru Li: methodology. Zhongfu Tan: methodology. Litong Dong: resources. Nian Mei: data analysis. Haiyou Wang: project administration.

Conflict of interest: The authors state no conflict of interest.

Data availability statement: All data generated or analyzed during this study are included in this published article.

References

[1] Press C. Fast pyrolysis of biomass. J Anal Appl Pyrolysis. 2017;6(2):95–135. doi: 10.1016/0165-2370(84)80008-X.
[2] Heidenreich S, Foscolo PU. New concepts in biomass gasification. Prog Energy Combust Sci. 2015;46:72–95. doi: 10.1016/j.pecs.2014.06.002.
[3] Raveendran K, Ganesh A. Heating value of biomass and biomass pyrolysis products. Fuel. 1996;75(15):1715–20. doi: 10.1016/S0016-2361(96)00158-5.
[4] Wang Y, Akbarzadeh A, Chong L, Du J, Tahir N, Awasthi MK. Catalytic pyrolysis of lignocellulosic biomass for bio-oil production: A review. Chemosphere. 2022;297(134181):1–15. doi: 10.1016/j.chemosphere.2022.134181.
[5] Namioka T, Saito A, Inoue Y, Park Y, Min TJ, Roh SA, et al. Hydrogen-rich gas production from waste plastics by pyrolysis and low-temperature steam reforming over a ruthenium catalyst. Appl Energy. 2011;88:2019–26. doi: 10.1016/j.apenergy.2010.12.053.
[6] Liu S, Wu G, Syed-Hassan S, Li B, Hu X, Zhou J, et al. Catalytic pyrolysis of pine wood over char-supported Fe: Bio-oil upgrading and catalyst regeneration by CO_2/H_2O. Fuel. 2022;307:121778. doi: 10.1016/j.fuel.2021.121778.
[7] Cordioli E, Patuzzi F, Baratieri M. Thermal and catalytic cracking of toluene using char from commercial gasification systems. Energies. 2019;12(19):1–16. doi: 10.3390/en12193764.
[8] Huang Y, Liu S, Akhtar MA, Li B, Zhou J, Zhang S, et al. Volatile-char interactions during biomass pyrolysis: Understanding the potential origin of char activity. Bioresour Technol. 2020;316:123938.
[9] Dahou T, Defoort F, Khiari B, Labaki M, Dupont C, Jeguirim M. Role of inorganics on the biomass char gasification reactivity: A review involving reaction mechanisms and kinetics models. Renew Sus Energy Rev. 2021;135:110136.
[10] And YO, Asami K. Ion-exchanged calcium from calcium carbonate and low-rank coals: High catalytic activity in steam gasification. Energy Fuels. 1996;10(2):431–5. doi: 10.1021/ef950174f.
[11] Ban Y, Liu Q, Zhou H, He R, Li N. Direct production of hydrogen-enriched syngas by calcium-catalyzed steam gasification of Shengli lignite/chars: Structural evolution. Int J Hydrog Energy. 2020;45(15):8357–68. doi: 10.1016/j.ijhydene.2020.01.018.
[12] Yang L, Yang H, Hu J, Wang X, Chen H. Effect of catalysts on the reactivity and structure evolution of char in petroleum coke steam gasification. Fuel. 2014;117(6):1174–80. doi: 10.1016/j.fuel.2013.08.066.
[13] Wang N, Chen D, Arena U, He P. Hot char-catalytic reforming of volatiles from MSW pyrolysis. Appl Energy. 2017;191(APR.1):111–24. doi: 10.1016/j.apenergy.2017.01.051.
[14] Park J, Lee Y, Ryu C. Reduction of primary tar vapor from biomass by hot char particles in fixed bed gasification. Biomass

Bioenergy. 2016;90:114–21. doi: 10.1016/j.biombioe.2016.04.001.
[15] Knudsen JN, Jensen PA, Dam-Johansen K. Transformation and release to the gas phase of Cl, K, and S during combustion of annual biomass. Energy Fuels. 2004;18(5):1385–99. doi: 10.1021/ef049944q.
[16] Jiang Y, Zong P, Bao Y, Zhang X, Wei H, Tian B, et al. Catalytic conversion of gaseous tar using coal char catalyst in the two-stage downer reactor. Energy. 2022;242:123013. doi: 10.1016/j.energy.2021.123013.
[17] Zhang S, Min Z, Tay H-L, Asadullah M, Li C-Z. Effects of volatile-char interactions on the evolution of char structure during the gasification of Victorian brown coal in steam. Fuel. 2011;90(4):1529–35. doi: 10.1016/j.fuel.2010.11.010.
[18] Gasson JR, Forchheim D, Sutter T, Hornung U, Kruse A, Barth T. Modeling the lignin degradation kinetics in an ethanol/formic acid solvolysis approach. Part 1. Kinetic model development. Ind Eng Chem Res. 2012;51(32):10595–606. doi: 10.1021/ie301487v.
[19] Bai Y, Zhu S, Kang L, Gao M, Fan L. Coal char gasification in H_2O/CO_2: Release of alkali and alkaline earth metallic species and their effects on reactivity. Appl Therm Eng. 2017;112:156–63. doi: 10.1016/j.applthermaleng.2016.10.044.
[20] Coates J. Interpretation of infrared spectra, a practical approach. New York: John Wiley & Sons, Ltd; 2006.
[21] Nasirudeen MB, Jauro A. Quality of some Nigerian coals as blending stock in metallurgical coke production. J Min Mater Charact Eng. 2011;10(1):101–9. doi: 10.4236/jmmce.2011.101007.
[22] Wu F, Tseng R, Juang R. Pore structure and adsorption performance of the activated carbons prepared from plum kernels. J Hazard Mater. 1999;69:287–302. doi: 10.1016/S0304-3894(99)00116-8.
[23] De Boer JH, Linsen BG, Van der Plas T, Zondervan GJ. Studies on pore systems in catalysts: VII. Description of the pore dimensions of carbon blacks by the t method. J Catal. 1965;4:649–53. doi: 10.1016/0021-9517(65)90264-2.
[24] Juang RS, Tseng RL, Wu FC. Role of microporosity of activated carbons on their adsorption abilities for phenols and dyes. Adsorpt Int Adsorpt Soc. 2001;7:65–72. doi: 10.1023/A:1011225001324.
[25] Arena U. Process and technological aspects of municipal solid waste gasification. A review. Waste Manage. 2012;32(4):625–39. doi: 10.1016/j.wasman.2011.09.025.
[26] Zhang S, Asadullah M, Dong L, Tay HL, Li CZ. An advanced biomass gasification technology with integrated catalytic hot gas cleaning. Part II: Tar reforming using char as a catalyst or as a catalyst support. Fuel. 2013;112:646–53. doi: 10.1016/j.fuel.2013.03.015.
[27] Chen M, Chen D, Arena U, Feng Y, Yu H. Treatment of volatile compounds from municipal solid waste pyrolysis to obtain high quality syngas: Effect of various scrubbing devices. Energy Fuels. 2017;31(12):13682–91. doi: 10.1021/acs.energyfuels.7b02388.
[28] MT/T 561-2008. Classification for fixed carbon of coal. 2008.
[29] Strakhov VM. Production of special coke for use in electric furnaces. Coke Chem. 2008;51:364–69. doi: 10.3103/S1068364X08090068.
[30] Funke A, Niebel A, Richter D, Abbas MM, Müller AK, Radloff S, et al. Fast pyrolysis char - assessment of alternative uses within the bioliq® concept. Bioresour Technol. 2016;200:905–13. doi: 10.1016/j.biortech.2015.11.012.
[31] Fatehi H, Bai XS. Structural evolution of biomass char and its effect on the gasification rate. Appl Energy. 2017;185(2):998–1006. doi: 10.1016/j.apenergy.2015.12.093.
[32] Li X, Hayashi JI, Li CZ. FT-Raman spectroscopic study of the evolution of char structure during the pyrolysis of a Victorian brown coal. Fuel. 2006;85(12/13):1700–7. doi: 10.1016/j.fuel.2006.03.008.
[33] Griffiths PR. The handbook of infrared and Raman characteristic frequencies of organic molecules. New York: Elsevier Inc; 1992.
[34] Wang Y, Alsmeyer DC, Mccreery RL. Raman spectroscopy of carbon materials: Structural basis of observed spectra. Chem Mater. 2002;2(5):557–63. doi: 10.1021/cm00011a018.
[35] Smith MW, Dallmeyer I, Johnson TJ, Brauer CS, Garcia-Perez M. Structural analysis of char by Raman spectroscopy: Improving band assignments through computational calculations from first principles. Carbon. 2016;100:678–92. doi: 10.1016/j.carbon.2016.01.031.
[36] Tamaddon F, Tayefi M, Hosseini E, Zare E. Dolomite (CaMg$(CO_3)_2$) as a recyclable natural catalyst in Henry, Knoevenagel, and Michael reactions. J Mol Catal A Chem. 2013;366:36–42. doi: 10.1016/j.molcata.2012.08.027.
[37] Bar-Ziv E, Zaida A, Salatino P, Senneca O. Diagnostics of carbon gasification by Raman microprobe spectroscopy. Proc Combust Inst. 2000;28(2):2369–74. doi: 10.1016/S0082-0784(00)80649-9.
[38] Sheng C. Char structure characterised by Raman spectroscopy and its correlations with combustion reactivity. Fuel. 2007;86(15):2316–24. doi: 10.1016/j.fuel.2007.01.029.
[39] Zaida A, Bar-Ziv E, Radovic LR, Lee YJ. Further development of Raman microprobe spectroscopy for characterization of char reactivity. Proc Combust Inst. 2007;31(2):1881–87. doi: 10.1016/j.proci.2006.07.011.
[40] Peng H, Yan K, Wu D, Zhou L, Liu Z, Li B, et al. Photochemical chlorination of graphene. ACS Nano. 2011;5:5957–64. doi: 10.1021/nn201731t.
[41] Sun Y, Gao S, Lei F, Xie Y. Atomically-thin two-dimensional sheets for understanding active sites in catalysis. Chem Soc Rev. 2015;44:623–36. doi: 10.1039/c4cs00236a.
[42] Xing J, Jiang HB, Chen JF, Li YH, Wu L, Yang S, et al. Active sites on hydrogen evolution photocatalyst. J Mater Chem A. 2013;1:15258–66. doi: 10.1039/C3TA13167J.
[43] Kibsgaard J, Chen Z, Reinecke BN, Jaramillo TF. Engineering the surface structure of MoS_2 to preferentially expose active edge sites for electrocatalysis. Nat Mater. 2012;11:963–9. doi: 10.1038/nmat3439.
[44] Behrens M, Studt F, Kasatkin I, Kühl S, Hävecker M, Abild-Pedersen F, et al. The active site of methanol synthesis over $Cu/ZnO/Al_2O_3$ Ind Catal. Sci. 2012;336:893–7. doi: 10.1126/science.1219831.
[45] Odeh AO. Qualitative and quantitative ATR-FTIR analysis and its application to coal char of different ranks. J Fuel Chem Tech. 2015;43(2):129–37. doi: 10.1016/S1872-5813(15)30001-3.
[46] Jin SC, Choi JC, Ko JH, Park YK, Park SH, Jeong KE, et al. The low-temperature SCR of NO over rice straw and sewage sludge derived char. Chem Eng J. 2010;156:321–7. doi: 10.1016/j.cej.2009.10.027.

[47] Xie YF, You JL, Lu LM, Wang M, Wang J. Raman spectroscopic study of coal samples during heating. Appl Sci. 2019;9:4699–707. doi: 10.3390/app9214699.
[48] Tong J, Han X, Wang S, Jiang X. Evaluation of structural characteristics of Huadian oil shale kerogen using direct techniques (solid-state 13 C NMR, XPS, FT-IR, and XRD). Energy Fuels. 2011;25:4006–13. doi: 10.1021/ef200738p.
[49] Yeboah YD, Longwell JP, Howard JB, Peters WA. Effect of calcined dolomite on the fluidized bed pyrolysis of coal. Ind Eng Chem Process Des Dev. 1980;19:646–53. doi: 10.1021/i260076a025.